PAPER

1D hollow tubular/2D nanosheet hybrid dimensional porous carbon prepared by one-step carbonization using natural minerals as templates for supercapacitors†

Fangfang Liu, [ID] [a] Chao Zhang,[a] Weiwei Huang,[a] Lei Chen,[a] Yuanshuang Wang,[a] Jinan Niu [ID] *[a] and Xiuyun Chuan*[b]

The reasonable construction of one-dimensional (1D)/two-dimensional (2D) hybrid dimensional porous carbon materials with complementary advantages and disadvantages is an important approach to addressing the structural and performance deficiencies of single carbon materials, while also significantly improving the electrochemical performance of super-capacitors. In this study, 1D hollow tubular/2D nanosheet hybrid dimensional porous carbon was synthesized through one-step carbonization using 1D fibrous brucite and 2D layered magnesium carbonate hydroxide as templates. By adjusting the feed ratio of 1D fibrous and 2D layered templates, the morphology, pore structure and specific surface area (SSA) of the prepared 1D hollow tubular/2D nanosheet hybrid dimensional porous carbon were controlled. The prepared hybrid dimensional porous carbons were characterized using scanning electron microscope (SEM), X-ray diffraction (XRD), X-ray photoelectron spectroscopy (XPS) and nitrogen adsorption–desorption. And their electrochemical performance was also studied by cyclic voltammograms (CV), galvanostatic charge/discharge (GCD) and electrochemical impedance spectroscopy (EIS). The results show that the use of templates with different dimensions significantly influences the morphology, pore structure, SSA and electrochemical performance of the synthesized hybrid dimensional porous carbon. The hybrid dimensional porous carbon (3F) exhibits a high specific capacitance and excellent cycling stability. 3F demonstrates the specific capacitance of 245.3 F g^{-1} at 1 A g^{-1}. Furthermore, the capacity retention rate remains as high as 93.4% after 8000 cycles at 10 A g^{-1}. This work reveals that hybrid dimensional porous carbon composed of 1D hollow carbon tubes and 2D carbon nanosheets has great potential for use in supercapacitor electrode materials.

1. Introduction

Since the 21st century, energy resource crises and environmental issues have become two major challenges that humanity must confront. The replacement of traditional energy sources with renewable and clean energy sources such as wind, hydrogen, and solar power has become the prevailing trend.[1,2] Simultaneously, emerging energy storage technologies like lithium ion batteries, sodium ion batteries, lithium–sulfur batteries, supercapacitors and so on have found excellent development opportunities.[3,4] Supercapacitors, with their advantages of high power density, long cycle life, rapid charge–discharge rates and eco-friendliness, hold significant potential

for a wide range of applications.[5,6] Nanostructured carbon-based materials such as carbon nanotubes (CNTs)[7] and graphene (G),[8] due to their low cost, environmental friendliness, abundant pore structure, large specific surface area, excellent thermal stability and chemical stability, are widely used as electrode materials for supercapacitors.[9] Among them, the hollow tubular structure of carbon nanotubes facilitates the rapid diffusion and migration of electrolyte ions, shows excellent directional conductivity and possesses certain spatial support capabilities, but it has poor charge storage capacity.[10] On the other hand, graphene has advantages such as thin thickness, short transmission distance, large SSA, exposure of abundant active sites on the surface, as well as excellent flexibility, conductivity and stability, but it tends to agglomerate, leading to a significant reduction in SSA and active sites.[11,12] These issues severely limit the application of individual carbon materials in electrode materials. Composite of two different dimensional carbon materials can complement each other's drawbacks, thereby realizing the synergistic play of their

[a]School of Materials Science and Physics, China University of Mining and Technology, Xuzhou, 221116, China. E-mail: jinan.niu@cumt.edu.cn

[b]Key Laboratory of Orogen Belts and Crustal Evolution, School of Earth and Space Sciences, Peking University, Beijing, 100871, China. E-mail: xychuan@pku.edu.cn

respective advantages. Therefore, the rational construction of hybrid dimensional porous carbon materials with complementary advantages and disadvantages is an important approach to address the structural and performance deficiencies of single carbon materials, which is of great significance for improving the performance of supercapacitors.

Currently, binary composite hybrid dimensional porous carbon materials are widely used in supercapacitor electrode materials.[13] Among them, the most common design strategy is to composite carbon nanotubes (CNT) with a special tubular structure and graphene (G) with excellent in-plane conductivity to prepare carbon nanotube/graphene (CNT/G) hybrid dimensional porous carbon materials. 1D carbon nanotubes can effectively inhibit the stacking aggregation of 2D graphene while increasing the distance between graphene layers. They can also construct a three-dimensional (3D) conductive network structure. Therefore, CNT/G hybrid dimensional porous carbon materials are favored by researchers.[14] Jiang et al.[15] prepared CNT/G composite materials through ascorbic acid-assisted reduction, freeze–drying and annealing using carbon nanotubes (CNT) and graphene (G) as precursors. In a 1 M Et_4NBF_4/PC electrolyte, the CNT/G//CNT/G symmetric supercapacitor exhibited a specific capacitance of 128 F g^{-1}, significantly higher than the 21.67 F g^{-1} of CNT//CNT. Lim et al.[16] synthesized CNT/G composite materials using Zn foil as an external initiator. Compared to graphene (G) without carbon nanotubes (CNT), CNT/G exhibited superior conductivity and higher specific capacitance. Li et al.[17] synthesized a self-supporting AC/CNT/G flexible composite material using a vacuum filtration method. It showed excellent electrochemical performance, with an energy density of up to 30 W h kg^{-1}, surpassing both individual carbon nanotubes and graphene. Numerous studies have shown that binary composite hybrid dimensional porous carbon materials exhibit superior electrochemical properties compared to individual carbon materials. However, to prepare carbon nanotubes and graphene separately faces challenges such as high energy consumption, complex processes, and low raw material utilisation.[18–20] These issues make it difficult to meet the demands for cost-effective and large-scale production of CNT/G hybrid dimensional porous carbon materials. However, in

nature, there are abundant 1D and 2D mineral resources that have advantages such as structural stability, abundant pores, low cost, and environmental friendliness.[21,22] Therefore, the direct synthesis of carbon nanotubes[23] and graphene[24] using 1D and 2D natural minerals as templates has attracted attention due to its simplicity, low cost and scalability.

Herein, this article aims to synthesize hybrid dimension porous carbons using 1D fibrous brucite and 2D layered magnesium carbonate hydroxide as templates, and polyvinyl pyrrolidone (PVP) as the carbon source, through a one-step high-temperature carbonization method (Fig. 1). Compared to the reported synthesis method of CNT/G hybrid dimension porous carbon materials, our synthesis method has significant advantages. Firstly, the synthesis of hybrid dimension porous carbon can be achieved with a simple and easy-to-operate one-step carbonization process. Secondly, the templates used are widely available, cost-effective, environmentally friendly, and in line with sustainable development strategies. In addition, the templates not only contribute to specific morphologies but also act as pore-forming agents. After template removal, the space occupied by the templates forms abundant pore channels, providing more active sites for electrolyte ions and convenient diffusion pathways. Lastly, a series of hybrid dimension porous carbons with different morphologies and pore structures are synthesized by adjusting the feeding ratio between the fibrous/layered templates of different dimensions. The effects of morphology, SSA, pore size distribution, and pore structure on the electrochemical performance are also studied.

2. Experimental section

2.1 Material

The fibrous brucite was sourced from the Ningqiang heimulin fibrous brucite in Hanzhong City, Shaanxi Province, China. The layered magnesium carbonate hydroxide ($Mg_2(OH)_2CO_3$) was purchased from Lorasa Chemical Corporation in the United States of America. Polyvinyl pyrrolidone (PVP, $(C_6H_9NO)_n$) was obtained from Aladdin biochemical technology Co., Ltd. Hydrochloric acid (HCl, AR) and hydrofluoric acid (HF, AR) were purchased from Nanjing chemical reagent Co., Ltd.
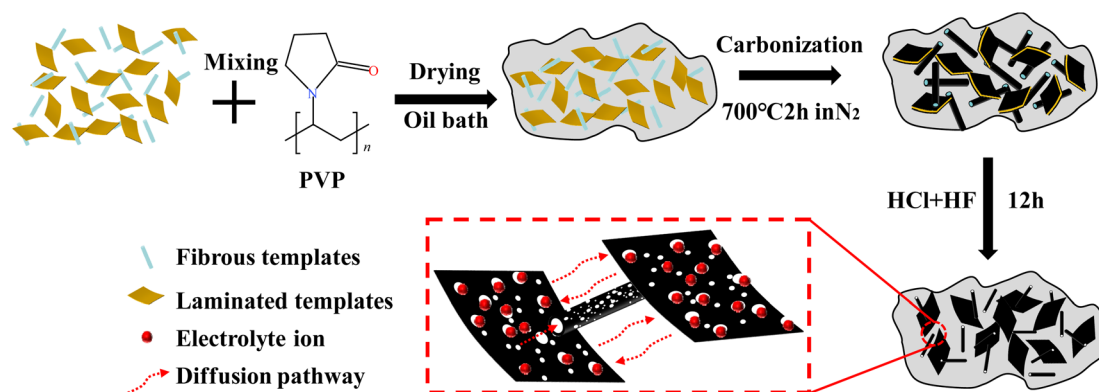

Fig. 1 Schematic illustration of synthesis of hybrid dimensional porous carbon.

2.2 Fabrication of binary composite hybrid dimensional porous carbon

A specific mass ratio of layered magnesium carbonate hydroxide $(Mg_2(OH)_2CO_3)$ and fibrous brucite was dispersed in 100 mL of deionized water. 4 g of PVP was added to the mixture and stirred at room temperature for 2 h. Then, ultrasonication was performed for 1 h. The resulting mixture was then stirred in an 80 °C oil bath until all the deionized water evaporated. The obtained template/carbon precursor was dried overnight in a 110 °C oven. The precursor was then transferred into a tube furnace under N_2 atmosphere. It was carbonized at 400 °C for 0.5 h and further heated at 700 °C for 2 h (5 °C min^{-1}). Then the template was removed by stirring in 1 M HCl and HF for 12 h each. The sample was subsequently washed with deionized water until neutral and dried in an 80 °C oven for 12 h, resulting in the final product, 1D hollow tube/2D layer hybrid dimensional porous carbon. When the mass combinations of fibrous brucite and layered magnesium carbonate hydroxide are 0.5 g and 3.5 g, 1.0 g and 3.0 g, 1.5 g and 2.5 g, 2.0 g and 2.0 g, 2.5 g and 1.5 g, 3.0 g and 1.0 g, and 3.5 g and 0.5 g, the resulting samples are respectively labeled as 0.5F, 1.0F, 1.5F, 2.0F, 2.5F, 3.0F and 3.5F. In addition, samples obtained with only fibrous brucite and only layered magnesium carbonate hydroxide are used as control experiments and labeled as 4.0F and 0F, respectively.

2.3 Material characterization

The phase characterization of hybrid dimensional porous carbon was performed using X-ray diffractometer (XRD, D8 Advance, BRUKER AXS, Germany) and laser confocal Raman spectrometer (Raman, Senterra, BRUKER, China). The specific surface area and pore structure of the samples were tested using the Brunauer–Emmett–Teller analyzer (BET, ASAP2020PLUS HD88, Micromeritics, USA). The morphology of the samples was observed using the scanning electron microscope (SEM, SU8220, Hitachi, Japan) and the field emission transmission electron microscope (FTEM, Tecnai G2 F20, Thermo Fisher Scientific, USA). The chemical elemental composition of the materials was obtained by scanning the local area of the material using an X-ray photoelectron spectrometer (XPS, ESCALAB250XI, Thermo Fisher Scientific, USA).

2.4 Electrochemical test

The electrochemical properties of hybrid dimensional porous carbon were tested using the Chenhua CHI660E electrochemical workstation. In the three-electrode system, the Hg/HgO and platinum sheet electrodes were used as the reference electrode and the counter electrode, respectively. While the synthesized sample was used as the working electrode. The electrolyte used was 6 M KOH. The preparation steps of the working electrode are as follows: the synthesized sample and conductive carbon black were mixed in a mass ratio of 8 : 1 in a mortar. Several drops of ethanol solution (volume ratio of anhydrous ethanol to deionized water is 1 : 1) were added, and the mixture was ground evenly. PTFE with the same mass as conductive carbon black was added, and the mixture was

ground again to obtain a homogeneous slurry. The slurry was coated on the foam nickel with dimensions of 10 × 20 × 1.5 mm, and then the coated foam nickel was placed in an 80 °C oven for 12 h. After drying, the foam nickel was pressed using a manual press machine (5 MPa pressure, 5 min pressing time) to obtain the working electrode. The active material was loaded at 1.2 mg cm^{-2}, and the specific capacitance was calculated based on the GCD curve using the following formula (1):[25]

$$C = \frac{I\Delta t}{m\Delta V} \tag{1}$$

$I(A)$ and $\Delta t(s)$ represent the discharge current and discharge time, respectively. $m(g)$ represents the mass of the active material, $\Delta V(V)$ represents the voltage window, and C (F g^{-1}) represents the specific capacitance. The testing content includes cyclic voltammograms (CV, voltage range: −0.6 to 0.2 V, scan rate: 5 to 200 mV s^{-1}), galvanostatic charge/discharge (GCD, voltage range: −0.6 to 0.2 V, current density: 0.5 to 10 A g^{-1}) and electrochemical impedance spectroscopy (EIS, frequency range: 10^{-2} to 10^5 Hz), and cycling stability (8000 cycles at 10 A g^{-1}).

In the two-electrode system, the prepared samples were used as both positive and negative electrodes, and 6 M KOH was used as the electrolyte to assemble a symmetric supercapacitor. The working electrode was prepared as follows: the active substance, PVDF (binder), and carbon black (conductive agent) were ground into a slurry according to the mass ratio of 8 : 1 : 1, and coated onto graphite paper, where NMP was the solvent. The loading of the active substance was 1.3 mg cm^{-2}. According to the GCD curve, the specific capacitance (C_s, F g^{-1}) of the single electrode was calculated according to formula (2), and the energy density (E_t, W h kg^{-1}) and power density (P_t, W kg^{-1}) were calculated according to formulas (3) and (4), respectively.

$$C_s = \frac{4I\Delta t}{m\Delta U} \tag{2}$$

$$E_t = \frac{C_t(\Delta U)^2}{2 \times 3.6} \tag{3}$$

$$P_t = \frac{E_t \times 3600}{\Delta t} \tag{4}$$

$I(A)$, $\Delta t(s)$ and $\Delta U(V)$ are the discharge current, discharge time and discharge voltage, respectively, and $m(g)$ is the mass of active material.

3. Results and discussion

3.1 Morphology and structure

Fig. 2a shows the XRD patterns of the 0F, 1F, 2F, 3F and 4F samples. There are two prominent peaks at around 28° and 41° which correspond to the (002) and (100) planes of graphite, respectively. In addition, the broad and weak peak in the pattern indicates the amorphous carbon nature of the sample.[26,27] No other diffraction peaks except for the amorphous carbon were observed, indicating the complete removal of the template and the absence of other impurities. The Raman
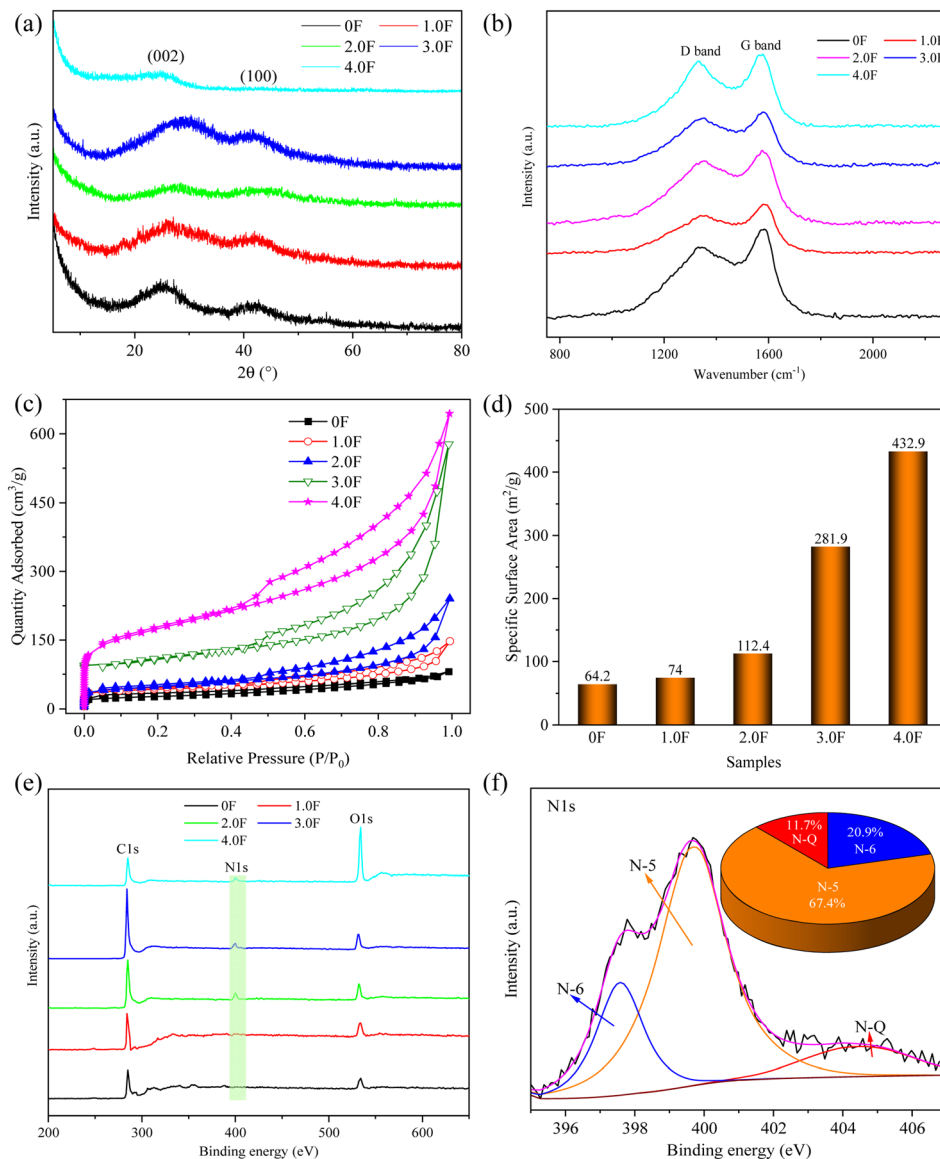
Fig. 2 (a) XRD; (b) Raman; (c) N_2 adsorption–desorption isotherms; (d) specific surface area; (e) XPS of hybrid dimension porous carbon and (f) N1s spectra of 3.0F.

spectra of the 0F, 1F, 2F, 3F and 4F samples are shown in Fig. 2b, and the peaks near 1335 cm^{-1} and 1581 cm^{-1} corresponding to the D band and the G band, respectively. As can be seen from the Fig. 2b, the integral area of the D peak is significantly larger than that of the G peak, indicating that the samples exhibits amorphous characteristics, which is consistent with the results demonstrated by the XRD pattern. Fig. 2c displays the N_2 adsorption–desorption isotherms of the 0F, 1F, 2F, 3F and 4F samples. All samples exhibit type IV isotherms with hysteresis loops, which can be attributed to the capillary condensation in the meso-pores.[28,29] The adsorption in low, medium and high pressure ranges indicates the co-existence of micro-pores, meso-pores, and macro-pores in the samples.[30,31] The hierarchical pore structure can significantly improve the electrochemical performance due to the contribution of micro-pores as active sites, meso-pores allowing for fast diffusion and

transport of electrolyte ions, and macro-pores serving as reservoirs for ion storage.[32] Fig. S1† shows the BJH pore size distribution, which exhibits the adsorption of all pore sizes including micro-pores, meso-pores, and macro-pores, but the overall adsorption of micro-pores is small, indicating a limited number of micro-pores in the sample. The SSA of the 0F, 1F, 2F, 3F and 4F samples are 64.2, 74.0, 112.4, 281.9 and 432.9 m^2 g^{-1}, respectively (Fig. 2d), which gradually increases with an increase in the 1D fibrous brucite template, possibly due to the contribution of the hollow carbon tube.

The elemental composition of 0F, 1F, 2F, 3F and 4F samples were analyzed using XPS. In Fig. 2e, the XPS survey spectrum reveals characteristic peaks around 284.21, 399.19 and 531.55 eV, corresponding to C, N and O, indicating *in situ* doping of nitrogen atoms during the carbonization process due to the thermal decomposition of PVP.[33] Additionally, the atomic

percentages of C, N and O elements of 3.0F are 84.51%, 4.41% and 11.09%, respectively. The N1s spectrum was deconvoluted into three peaks labeled as pyridinic-N (N-6), pyrrolic-N (N-5) and graphitic-N (N-Q), located at 397.57, 399.66 and 404.34 eV, respectively.[34–36] The nitrogen content for N-6, N-5 and N-Q is 20.9%, 67.4% and 11.7%, respectively (Fig. 2f). Among them, N-6 and N-5 are situated at the edge of the carbon framework, providing additional active sites and pseudo-capacitance, while N-Q involves nitrogen atoms replacing carbon atoms within the carbon framework, significantly improving the conductivity of the carbon material.[37,38] Therefore, the introduction of nitrogen enhances the electrochemical performance of the porous carbon material.

Observation of the morphology and microstructure of the sample was carried out using SEM and TEM. Fig. 3a shows the SEM image of the porous carbon (0F) synthesized solely with 2D layered magnesium carbonate hydroxide as the template. It contains a large number of 2D nanosheets, but the nanosheets are severely aggregated and densely packed together. SEM images of a series of hybrid dimensional porous carbons (0.5F–3.5F) synthesized with fibrous/layer templates of different dimensions are shown in Fig. 3b–h. It can be seen that both 2D carbon nanosheets and 1D hollow carbon tubes are present in the hybrid dimensional porous carbons, forming a composite carbon material with 1D and 2D dimensions. The 1D carbon tubes provide convenient channels for the rapid transport of electrolyte ions and effectively prevent the aggregation of 2D carbon nanosheets. At the same time, with the increase of fibrous brucite template, the content of 1D carbon tubes in the

samples also gradually increases. In the SEM image of the 0.5F sample, 2D carbon nanosheets are mainly present, with a few scattered 1D carbon tubes (Fig. 3b). Fig. 3c–e show that the 2D carbon nanosheets are interlinked, but the distribution of 1D carbon tubes can be clearly seen. With the continued increase of the fibrous template, the 2.5F–3.5F samples are mainly composed of 1D carbon tubes, with a small amount of 2D carbon nanosheets. The porous carbon (4F) synthesized solely with 1D fibrous brucite as the template exhibits a 3D network structure formed by the interlinked 1D carbon tubes (Fig. 3i). The 1D carbon tubes in the hybrid dimensional porous carbon provide convenient channels for the rapid transport of electrolyte ions and effectively prevent the aggregation of 2D carbon nanosheets. TEM characterization further confirms the presence of stacked 1D hollow carbon tubes and a small amount of carbon nanosheets in the 3.0F sample (Fig. 4a and b), indicating that 3.0F is a hybrid dimensional porous carbon consisting of both 1D carbon tubes and 2D carbon nanosheets, consistent with the results of SEM images. High-resolution transmission electron microscopy (HRTEM) patterns are shown in Fig. 4c, and the inset is a selection of electron diffraction, all showing amorphous features. The uniform distribution of nitrogen (N) and oxygen (O) elements on the surface of the 3.0F sample is shown in Fig. 4d–f, indicating the *in situ* doping of N element during the carbonization process.

3.2 Electrochemical properties

The electrochemical performance of hybrid dimension porous carbon was evaluated through GCD, CV and EIS tests. Fig. S2†
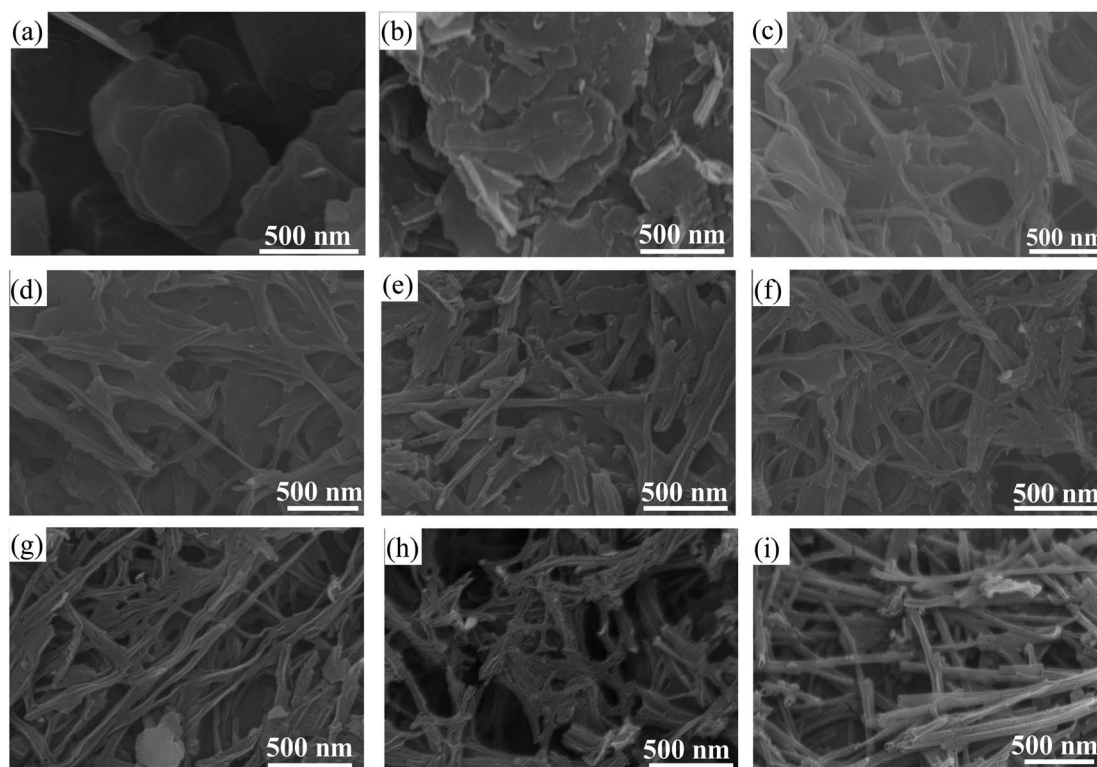

Fig. 3 SEM images of hybrid dimension porous carbon. (a) 0F; (b) 0.5F; (c) 1.0F; (d) 1.5F; (e) 2.0F; (f) 2.5F; (g) 3.0F; (h) 3.5F; (i) 4.0F.
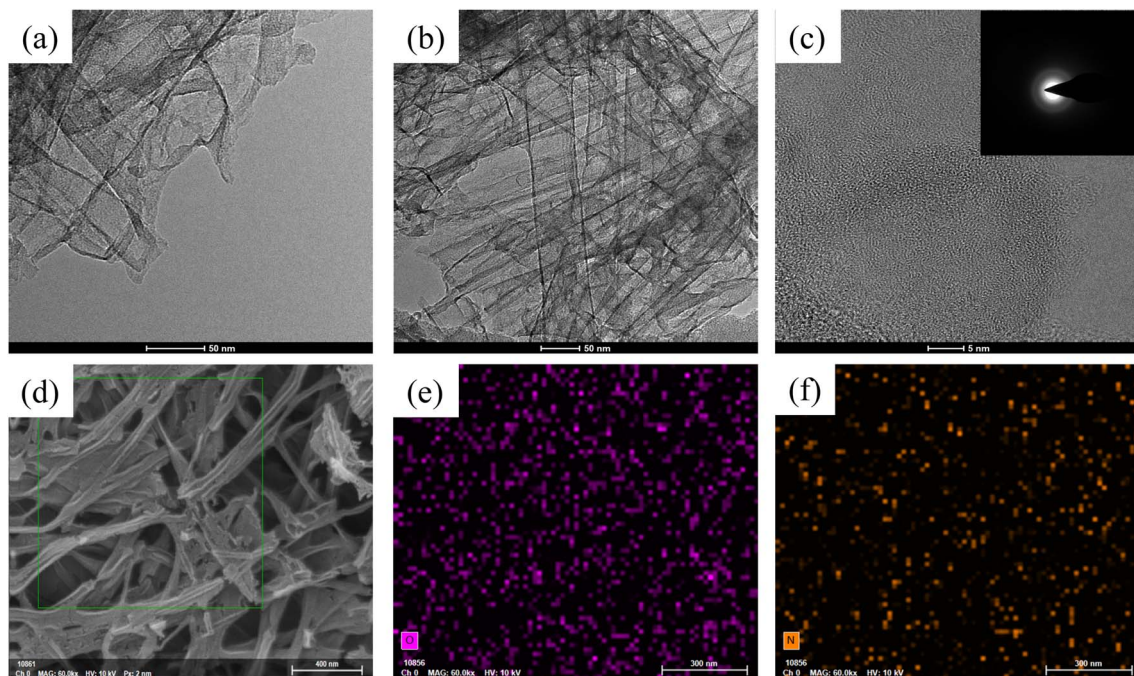
Fig. 4   (a and b) TEM images, (c) HRTEM (the inset shows the SAED pattern) and (d–f) elemental mapping images (N and O) of 3.0F.

shows the GCD curves of the 0F to 4.0F samples. GCD curves of all samples exhibited nearly isosceles triangle within the current density range of 0.5 to 10 A g^{-1}, indicating excellent double-layer capacitance characteristics of the hybrid dimension porous carbon. Fig. S3† presents the CV curves of the 0F to 4.0F samples at scan rates ranging from 5 to 200 mV s^{-1}. Even at 200 mV s^{-1}, the shape of the CV curves remained unchanged, exhibiting quasi-rectangular shapes, indicating good reversibility and double-layer capacitance characteristics of the hybrid dimensional porous carbon, consistent with the GCD results. Fig. 5 displays the electrochemical performance of the samples. At 1 A g^{-1}, the GCD curves of the 0F to 4F samples showed nearly isosceles triangular shapes with good symmetry and linearity, indicating excellent reversibility (Fig. 5a). Furthermore, the 3F sample exhibited the longest discharge time and had the highest specific capacitance calculated based on specific capacitance calculation formula (1). Fig. 5b shows the CV of the samples at 100 mV s^{-1}, all exhibiting rectangular shapes without redox peaks, indicating good double-layer capacitance characteristics. Additionally, the 3F sample had the largest area, indicating the highest specific capacitance, consistent with the GCD results.

In addition, the mass-specific capacitances calculated based on the GCD curves using the specific capacitance calculation formula (1) are shown in Fig. 5c. At 1 A g^{-1}, the mass-specific capacitances of the 0F, 0.5F, 1.0F, 1.5F, 2.0F, 2.5F, 3.0F, 3.5F and 4.0F samples were 75.63, 132.4, 134.9, 142.6, 149.0, 181.6, 245.3, 234.5 and 210.25 F g^{-1}, respectively. As shown in Fig. 5c, the 0F sample synthesized with layered template had the smallest specific capacitance, and the specific capacitance of the samples increased and then decreased with the addition of fibrous template. Table 1 presents the electrochemical

performance of some reported CNT/G binary composite porous carbons. It can be observed that the 3.0F sample prepared in this study exhibits notably excellent electrochemical properties. To further characterize the electrochemical performance of the samples, EIS tests were conducted, and the Nyquist plots are shown in Fig. 5d. The Nyquist plots of the samples were composed of a semicircle in the high-frequency region and a line in the middle-to-low-frequency region. The semicircle diameter in the high-frequency region represented the charge transfer resistance (R_{ct}), and the slope of the line in the low-frequency region represented the Warburg impedance (W_0). The larger the slope, the smaller the Warburg impedance. Fig. 5e shows an enlarged view of the high-frequency region of the Nyquist plots. The intercept of the curve with the X-axis represented the equivalent series resistance (R_s), and it can be observed that the R_s (0.5–0.75 Ω) and R_{ct} of the 0.5F to 4.0F samples were relatively small, while the R_s of the 0F sample was larger, with a value of 1.93 Ω. This is likely mainly due to the presence of hollow carbon tubes providing convenient channels for the fast diffusion and transport of electrolyte ions, resulting in a smaller R_s of the hybrid dimensional porous carbon. The cycle stability of the samples after 8000 cycles at 10 A g^{-1} is shown in Fig. 5f. The capacity retentions of the 0F, 0.5F, 1.0F, 1.5F, 2.0F, 2.5F, 3.0F, 3.5F and 4.0F samples were 98.6%, 98.9%, 97.2%, 98.8%, 95.3%, 96.4%, 93.4%, 95.5% and 95.6%, respectively. The capacity retentions remained above 90% after 8000 cycles, indicating excellent cycle stability of the hybrid dimension porous carbon.

To further characterize the diffusion kinetics of the hybrid dimensional porous carbon during charge and discharge processes, we employed formulas (S1) and (S2)† for evaluation. According to formula (S1),† the calculated b value of the 3.0F
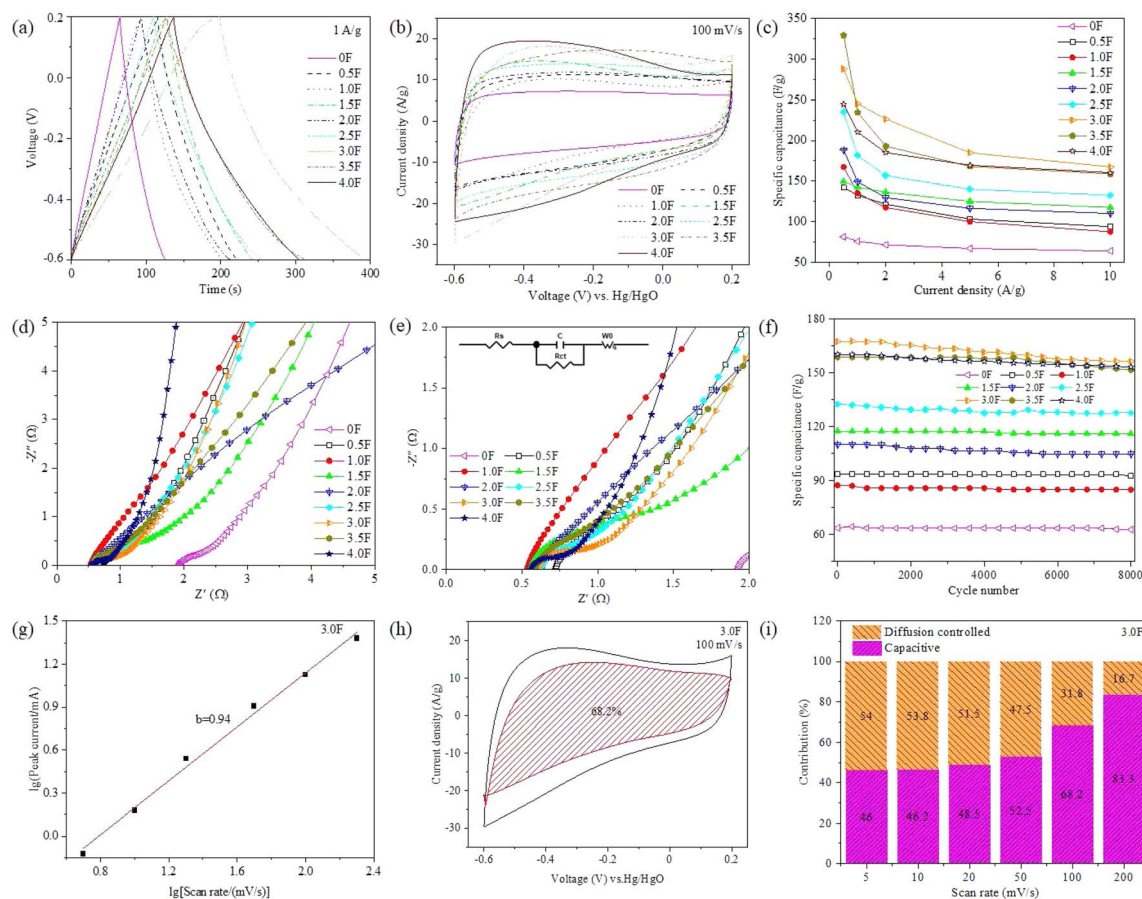
Fig. 5 The electrochemical performance of hybrid dimension porous carbon. (a) GCD curves at 1 A g^{-1}; (b) CV curves at 100 mV s^{-1}; (c) specific capacitance at different current density; (d) Nyquist plots; (e) the enlarged view of the high-frequency region of the Nyquist plots; (f) cycle stability; (g) determination of *b* value of 3.0F by CV curves of 5–200 mV s; surface-controlled capacitance at (h) 100 mV s^{-1}; (i) different scan rates.

Table 1 Comparison of the electrochemical performance of hybrid dimension porous carbon

Materials	Electrolyte	Capacitance (F g^{-1})	Cycle stability	Ref.
NC-M3-0.02	6 M KOH	137.1 at 0.5 A g^{-1}	104% after 5000 cycles	39
PEI-GN	1 M H$_2$SO$_4$	120 at 1 V s^{-1}	—	40
CNT/RGO	1 M Et$_4$NBF$_4$/PC	128 at 3.4 A g^{-1}	95.63% after 2000 cycles	15
AC/CNT/RGO	1 M LiClO$_4$	101 at 0.2 A g^{-1}	75% after 1000 cycles	17
RMGO-8	EMI-BF$_4$	213 at 0.2 A g^{-1}	—	41
3F	6 M KOH	245.3 at 1 A g^{-1}	93.4% after 8000 cycles	This work

sample is 0.94, indicating its demonstration of a double-layer capacitance behavior with ultrafast kinetic response. Additionally, utilizing formula (S2),† we calculated the capacitive contributions under surface-controlled and diffusion-controlled conditions at different scan rates. Fig. 5h and S4† display the capacitance contributions of 0F–4.0F samples at a scan rate of 100 mV s^{-1}, which are 86.5%, 80.6%, 68.2%, 78.7%, 87.5%, 88.0%, 68.2%, 84.6% and 85.6%, respectively. Furthermore, the capacitance contributions of 0F–4.0F samples at different scan rates of 5, 10, 20, 50, 100 and 200 mV s^{-1} are illustrated in Fig. 5i and S5.† At higher scan rates (200 mV s^{-1}),

the capacitive contribution is predominantly governed by surface control.

To further evaluate the capacitive behavior of the hybrid dimensional porous carbon, two-electrode symmetric capacitors were assembled using 6 M KOH as the electrolyte. The GCD curves of all the samples (Fig. S6† and 6a) showed good isosceles triangular shaped traits, indicating excellent double layer capacitance properties and reversibility of charging and discharging. Fig. 6b shows the GCD curves of different hybrid dimensional porous carbons at 1 A g^{-1} current density, and it can be seen that 3.0F//3.0F presents the longest discharge time, indicating that it has the maximum mass specific capacitance.
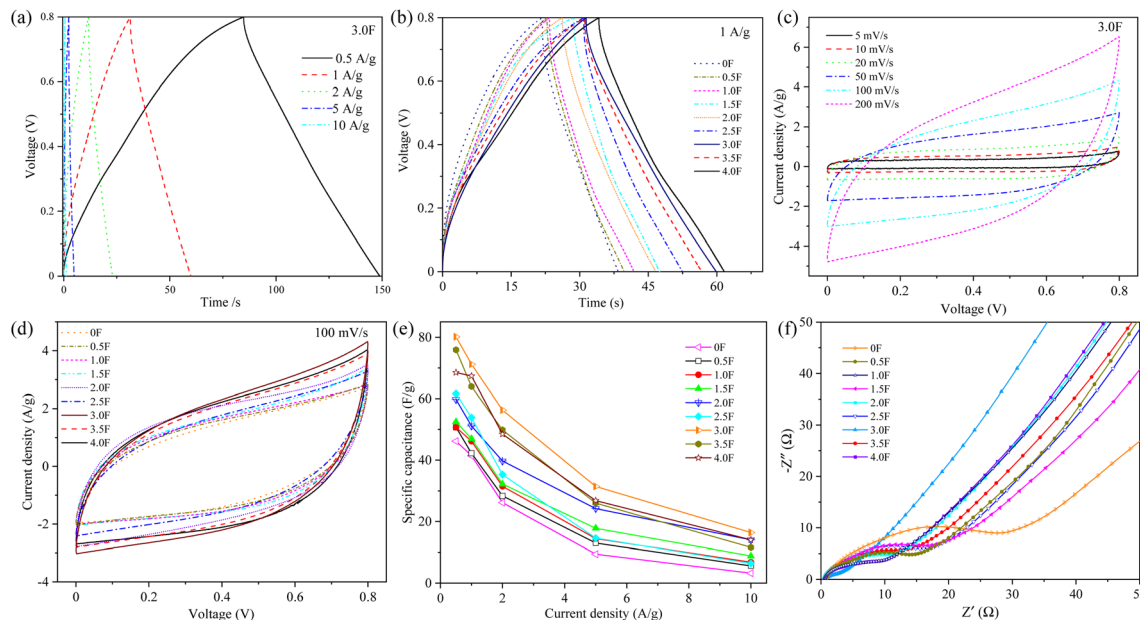
Fig. 6   The electrochemical performance of symmetric capacitors. (a) GCD curves at different current density of 3.0F//3.0F; (b) GCD curves of hybrid dimension porous carbon at 1 A g^{-1}; (c) CV curves at various scan rate of 3.0F//3.0F; (d) CV curves at 100 mV s^{-1}; (e) specific capacitance at different current density; (f) Nyquist plots.

The GCD curves of all the samples are shown in Fig. 6c and S7,† which exhibit a quasi-rectangular nature and remain undistorted as the scan rate increases, indicating that all the samples have excellent charge/discharge reversibility and good double layer capacitance behavior. Fig. 6d shows the CV curves of the samples at a scan rate of 100 mV s^{-1}. It can be seen that 3.0F//3.0F has the largest integrated area, qualitatively indicating that it has the largest specific capacitance, which is consistent with the results exhibited by the GCD curve. Based on the GCD curves, the specific capacitances at different current densities obtained by using formula (2) are shown in Fig. 6e, where 0F// 0F, 0.5F//0.5F, 1.0F//1.0F, 1.5F//1.5F, 2.0F//2.0F, 2.5F//2.5F, 3.0F//3.0F, 3.5F//3.5F and 4.0F//4.0F with specific capacitances of 46.17, 50.7, 50.7, 52.5, 59.76, 61.65, 80.13, 75.88 and 68.5 F g^{-1}, respectively. In order to further evaluate the electrochemical properties of the porous carbon, AC impedance tests were performed (Fig. 6f). The Nyquist plots of all samples consisted of semicircles in the high frequency region and straight lines in the middle and low frequency regions. The diameter of the semicircle represents the charge transfer resistance (R_{ct}), and the slope of the straight line represents the Warburg impedance, where the larger the slope, the smaller the impedance. From the Fig. 6f, it can be seen that 3.0F//3.0F has the smallest charge transfer resistance and Warburg impedance, which indicates that the electrolyte ions can be transported more conveniently inside the electrolyte, and therefore further indicates that it has excellent electrochemical performance.

4.   Conclusion

The hollow tubular/layered hybrid dimension porous carbon was synthesized directly through one-step carbonization using fibrous/layered hybrid template. This method is simple, easy to

operate, and cost-effective. The combination of two different dimensional porous carbon materials can compensate for the shortcomings of single-dimensional carbon materials and achieve synergistic effects of their respective advantages. Therefore, constructing hybrid dimension porous carbon materials with complementary advantages and disadvantages can significantly improve the electrochemical performance of carbon materials. Thanks to the abundant pore structure, hierarchical pore channels, and hollow tubular/layer composite morphology, the 3F sample exhibited a specific capacitance of 287.8 F g^{-1} (at 0.5 A g^{-1}), higher than that of 1D hollow tubular porous carbon (244.75 F g^{-1}) and 2D layer porous carbon (81.25 F g^{-1}). Therefore, the application of hybrid dimension porous carbon provides a short process and low-cost solution for high-performance super-capacitors.

Data availability

No data was used for the research described in the article.

Conflicts of interest

The authors declare no conflict of interest.

Acknowledgements

References

1 J. Cui, Z.-X. Zhang, H. Quan, Y. Hu, S. Wang and D. Chen, Effect of various ammonium salts as activating additive on

the capacitance performance of hierarchical porous carbon derived from camellia husk, *J. Energy Storage*, 2022, **51**, 104347.

2 S. Wang, D. Chen, Z.-X. Zhang, Y. Hu and H. Quan, Mesopore dominated capacitive deionization of N-doped hierarchically porous carbon for water purification, *Sep. Purif. Technol.*, 2022, **290**, 120912.

3 H. Jin, X. Feng, J. Li, M. Li, Y. Xia, Y. Yuan, C. Yang, B. Dai, Z. Lin, J. Wang, J. Lu and S. Wang, Heteroatom-doped porous carbon materials with unprecedented high volumetric capacitive performance, *Angew. Chem., Int. Ed.*, 2019, **58**(8), 2397–2401.

4 G. G. Bizuneh, A. M. M. Adam and J. Ma, Progress on carbon for electrochemical capacitors, *Battery Energy*, 2023, **2**(1), 20220021.

5 M. Zhang, N. Zhao and X. Li, The synthesis of carbon microspheres film composed of nano-onions and its application as flexible supercapacitors, *Carbon Energy*, 2021, **3**(3), 509–518.

6 C. Shao, S. Qiu, G. Wu, B. Cui, H. Chu, Y. Zou, C. Xiang, F. Xu and L. Sun, Rambutan-like hierarchically porous carbon microsphere as electrode material for high-performance supercapacitors, *Carbon Energy*, 2021, **3**(2), 361–374.

7 J. Zhang, H. Zhao, J. Li, H. Jin, X. Yu, Y. Lei and S. Wang, *In situ* encapsulation of iron complex nanoparticles into biomass-derived heteroatom-enriched carbon nanotubes for high-performance supercapacitors, *Adv. Energy Mater.*, 2019, **9**(4), 1803221.

8 D. Wang, L. Sheng, M. Jiang, X. Jin, X. Lin, S.-Y. Lee, J. Shi and W. Chen, Density and porosity optimization of graphene monoliths with high mass-loading for high-volumetric-capacitance electrodes, *Battery Energy*, 2022, **1**(4), 20220017.

9 M. Zhong, M. Zhang and X. Li, Carbon nanomaterials and their composites for supercapacitors, *Carbon Energy*, 2022, **4**(5), 950–985.

10 Y. Sheng, C. Li, J. Wang, X. Xia, G. J. Weng and Y. Su, Multiscale modeling of thermal conductivity of hierarchical CNT-polymer nanocomposite system with progressive agglomeration, *Carbon*, 2023, **201**, 785–795.

11 M. S. Shruti, S. Khilari, E. J. J. Samuel, H. Han and A. K. Nayak, Recent trends in graphene assisted vanadium based nanocomposites for supercapacitor applications, *J. Energy Storage*, 2023, **63**, 107006.

12 S. Park, S. H. Choi, J. M. Kim, S. Ji, S. Kang, S. Yim, S. Myung, S. K. Kim, S. S. Lee and K.-S. An, Nanoarchitectonics of MXene derived TiO_2/graphene with vertical alignment for achieving the enhanced supercapacitor performance, *Small*, 2023, 2305311.

13 Y. Hu, H. Quan, J. Cui, W. Luo, W. Zeng and D. Chen, Carbon nanodot modified N, O-doped porous carbon for solid-state supercapacitor: a comparative study with carbon nanotube and graphene oxide, *J. Alloys Compd.*, 2021, **877**, 160237.

14 X. Wu, F. Mu and H. Zhao, Recent progress in the synthesis of graphene/CNT composites and the energy-related applications, *J. Mater. Sci. Technol.*, 2020, **55**, 16–34.

15 L. Jiang, Q. Jiang, Q. Liu, J. Peng, Y. Gao, Z. Duan, A. Hu and X. Lu, Preparation of CNT/RGO macroscopic body by partially stripping CNT and its energy storage performances, *Diamond Relat. Mater.*, 2018, **88**, 1–5.

16 S. H. Kang, G. Y. Lee, J. Lim and S. O. Kim, CNT–rGO hydrogel-integrated fabric composite synthesized *via* an interfacial gelation process for wearable supercapacitor electrodes, *ACS Omega*, 2021, **6**(30), 19578–19585.

17 X. Li, Y. Tang, J. Song, W. Yang, M. Wang, C. Zhu, W. Zhao, J. Zheng and Y. Lin, Self-supporting activated carbon/carbon nanotube/reduced graphene oxide flexible electrode for high performance supercapacitor, *Carbon*, 2018, **129**, 236–244.

18 S. K. Soni, B. Thomas and V. R. Kar, A comprehensive review on CNTs and CNT-reinforced composites: syntheses, characteristics and applications, *Mater. Today Commun.*, 2020, **25**, 101546.

19 S. Rathinavel, K. Priyadharshini and D. Panda, A review on carbon nanotube: an overview of synthesis, properties, functionalization, characterization, and the application, *Mater. Sci. Eng., B*, 2021, **268**, 115095.

20 K. M. Wyss, D. X. Luong and J. M. Tour, Large-scale syntheses of 2D materials: flash joule heating and other methods, *Adv. Mater.*, 2022, **34**(8), 2106970.

21 X. Tang, R. Tang, S. Xiong, J. Zheng, L. Li, Z. Zhou, D. Gong, Y. Deng, L. Su and C. Liao, Application of natural minerals in photocatalytic degradation of organic pollutants: a review, *Sci. Total Environ.*, 2022, **812**, 152434.

22 L. Yang, X. Yang, F. Xia, Y. Gong, F. Li, J. Yu, T. Gao and Y. Li, Recent progress on natural clay minerals for lithium–sulfur batteries, *Chem. – Asian J.*, 2023, **18**(16), e202300473.

23 L. Zhong, A. Tang, P. Yan, J. Wang, Q. Wang, X. Wen and Y. Cui, Palygorskite-template amorphous carbon nanotubes as a superior adsorbent for removal of dyes from aqueous solutions, *J. Colloid Interface Sci.*, 2019, **537**, 450–457.

24 J. Sun, H. Liu, X. Chen, D. G. Evans, W. Yang and X. Duan, Synthesis of graphene nanosheets with good control over the number of layers within the two-dimensional galleries of layered double hydroxides, *Chem. Commun.*, 2012, **48**(65), 8126–8128.

25 W. Chen, H. Quan, X. Chen, H. Wang and D. Chen, Carbon quantum dot regulated electrochemical activation of $Co_{0.03}Ni_{0.97}LDH$ for energy storage, *Inorg. Chem. Front.*, 2024, **11**(3), 899–911.

26 N. Daems, J. Wouters, C. Van Goethem, K. Baert, C. Poleunis, A. Delcorte, A. Hubin, I. F. J. Vankelecom and P. P. Pescarmona, Selective reduction of nitrobenzene to aniline over electrocatalysts based on nitrogen-doped carbons containing non-noble metals, *Appl. Catal., B*, 2018, **226**, 509–522.

27 C. Yang, T. Zhao, H. Pan, F. Liu, J. Cao and Q. Lin, Facile preparation of N-doped porous carbon from chitosan and $NaNH_2$ for CO_2 adsorption and conversion, *Chem. Eng. J.*, 2022, **432**, 134347.

28 P. Jiang, K. Jiang, D. Tranca, J. Zhu, F. Qiu, C. Ke, C. Lu, E. Kymakis and X. Zhuang, Rational control of topological

defects in porous carbon for high-efficiency carbon dioxide conversion, *Adv. Mater. Interfaces*, 2021, **8**(7), 2100051.

29 M. Thommes, K. Kaneko, A. V. Neimark, J. P. Olivier, F. Rodriguez-Reinoso, J. Rouquerol and K. S. W. Sing, Physisorption of gases, with special reference to the evaluation of surface area and pore size distribution (IUPAC technical report), *Pure Appl. Chem.*, 2015, **87**(9–10), 1051–1069.

30 V. Jiménez, A. Ramírez-Lucas, J. A. Díaz, P. Sánchez and A. Romero, CO_2 capture in different carbon materials, *Environ. Sci. Technol.*, 2012, **46**(13), 7407–7414.

31 B. Gang, F. Zhang, X. Li, B. Zhai, X. Wang and Y. Song, A *Ulva lactuca*-derived porous carbon for high-performance electrode materials in supercapacitor: synergistic effect of porous structure and graphitization degree, *J. Energy Storage*, 2021, **33**, 102132.

32 L.-H. Zheng, M.-H. Chen, S.-X. Liang and Q.-F. Lü, Oxygen-rich hierarchical porous carbon derived from biomass waste-kapok flower for supercapacitor electrode, *Diamond Relat. Mater.*, 2021, **113**, 108267.

33 N. Wang, M. Wang, H. Quan, S. Wang and D. Chen, Waste *Camellia oleifera* shell-derived hierarchically porous carbon modified by Fe_3O_4 nanoparticles for capacitive removal of heavy metal ions, *Sep. Purif. Technol.*, 2024, **329**, 125184.

34 J. Wang, Y. Huang, Y. Gao, J. Dai and X. Sun, The construction of carbon nanofiber composites modified by graphene/polypyrrole for flexible supercapacitors, *J. Energy Storage*, 2022, **51**, 104581.

35 Y. Gao, J. Wang, Y. Huang, S. Zhang, S. Zhang and J. Zou, Rational design of N-doped porous biomass carbon nanofiber electrodes for flexible asymmetric supercapacitors with high-performance, *Appl. Surf. Sci.*, 2023, **638**, 158137.

36 H. Quan, X. Fan, W. Wang, W. Gao, Y. Dong and D. Chen, Hierarchically porous carbon derived from biomass: effect of mesopore and heteroatom-doping on electrochemical performance, *Appl. Surf. Sci.*, 2018, **460**, 8–16.

37 F. Liu, J. Niu, X. Chuan and Y. Zhao, Nitrogen and sulfur co-doping carbon in different dimensions as electrode for supercapacitor applications, *J. Alloys Compd.*, 2023, **947**, 169654.

38 F. Liu, X. Chuan, B. Li and P. Qi, One-step carbonization synthesis of *in situ* nitrogen-doped carbon tubes using fibrous brucite as the template for supercapacitors, *Mater. Chem. Phys.*, 2022, **281**, 125811.

39 Y. Zhang, M. Wang, J. Zhao, Y. Feng and J. Mi, Preparation and electrochemical properties of nitrogen-doped graphene/carbon nanotubes/amorphous carbon composites, *Chem. Ind. Eng. Prog.*, 2022, **41**(10), 5501–5509.

40 D. Yu and L. Dai, Self-assembled graphene/carbon nanotube hybrid films for supercapacitors, *J. Phys. Chem. Lett.*, 2010, **1**(2), 467–470.

41 J. Li, J. Tang, J. Yuan, K. Zhang, X. Yu, Y. Sun, H. Zhang and L.-C. Qin, Porous carbon nanotube/graphene composites for high-performance supercapacitors, *Chem. Phys. Lett.*, 2018, **693**, 60–65.